Experimental characterization of oscillations in the Magnetic Nozzle of an Electron Cyclotron Resonance Thruster

IEPC-2024-315

Presented at the 38th International Electric Propulsion Conference, Toulouse, France
June 23-28, 2024

Davide Maddaloni*
Aerospace Engineering Department, Universidad Carlos III de Madrid, Leganés, Madrid, Spain

Federico Boni, Victor Désangles
Physics Instrumentation and Space Department, ONERA, Université Paris-Saclay, 91123 Palaiseau, France

Borja Bayón-Buján, Mario Merino,
Aerospace Engineering Department, Universidad Carlos III de Madrid, Leganés, Madrid, Spain

and

Filippo Terragni
G. Millán Institute and Department of Mathematics, Universidad Carlos III de Madrid, Leganés, Madrid, Spain

Plasma oscillations in the range 5–100 kHz are experimentally observed in the plume of a coaxial electron cyclotron resonance thruster for different operating conditions of input microwave power, injected xenon flowrate, and microwave driving frequency. Data is collected by means of three independent diagnostics synchronized together: an array of 4 Langmuir probes, a microwave resonant curling probe, and a high-speed camera. Forward and reflected microwave power, as well as the thruster floating potential, are also recorded. Two oscillating dynamics are detected, one at lower frequencies, falling within the 5–12 kHz range, and another at higher frequencies, typically around 60 kHz. Their dependency upon changes of the inspected spatial position and thruster operating conditions is discussed. The waves are characterized using data-driven algorithms, and their suspected nature is preliminary discussed.

I. Introduction

Electrodeless plasma thruster (EPT) technologies are motivated by their ability to function without external cathodes and to allow for the use of alternative propellants with easiness. Nevertheless, the technological readiness level (TRL) of EPTs is still low in general, as are the demonstrated thrust efficiencies [1, 2, 3]. Electron cyclotron resonance thrusters (ECRTs) [4, 5, 6] exemplify one of the most promising instances of EPTs, achieving ionization using microwaves to excite the electrons at their cyclotron resonance frequency. Efficiencies of up to 50% have been reported on ECRTs [7] as of late.

In ECRTs, energy is transferred to the plasma through externally-applied electromagnetic fields. Downstream from the plasma source, a diverging magnetic field $\mathbf{B}$, often referred to as magnetic nozzle (MN) [8], confines and accelerates the plasma. Azimuthal electron currents interact with the applied field resulting in a radially-confining and downstream-accelerating force, while an ambipolar electric field $\mathbf{E}$ arises in the expanding plasma to maintain charge neutrality, which confines electrons and accelerates ions axially, generating thrust. The plasma in the MN is characterized by having a strong azimuthal relative drift between the

*PhD candidate, dmaddalo@ing.uc3m.es.

essentially-unmagnetized ions and the well-magnetized electrons, resulting from the combination of $\mathbf{E} \times \mathbf{B}$, ∇p_e, and $\nabla \mathbf{B}$ drifts, with p_e the electron pressure. Overall, the expanding plasma in a MN may be classified as an $\mathbf{E} \times \mathbf{B}$ discharge.

The study of oscillations in $\mathbf{E} \times \mathbf{B}$ plasmas has always been a quite active branch of the community. The development of instabilities, and/or turbulence, can affect particle transport across magnetic field lines, which in turn has the potential to compromise plasma confinement [9, 10, 11], but could also provide a means for effective electron detachment from the MN closed field lines [12, 13]. In MNs, control of the plasma confinement is crucial to ensure optimal mass utilization of the propulsion system and enhance total efficiency [14]. Hence, the lack of a comprehensive understanding of the physics can undermine the optimization of designs and predictive tools alike. Moreover, the presence of oscillations in the plume region may be regarded in some cases as the tell-tale of instabilities within the plasma source, which could drive plasma losses to the walls, and therefore have a direct impact on the propulsive performances of the device.

In Helicon plasma sources, evidence of cross electron transport being affected by non-linear interaction of drift wave turbulence with zonal flows and other plasma oscillations is abundant [15, 16, 17]. In these devices, the drift wave turbulence has been suggested to arise from coherent fluctuations of plasma density and plasma potential, gradually transitioning into broadband, turbulent structures possessing azimuthal propagation when the magnetic field intensity is increased [18, 19]. In ECR plasma sources, the existence of oscillations addressed to similar mechanisms has been observed as well [20], whereas other authors reported the existence of low frequency oscillations linked to ionization processes [21]. In Hall thrusters, the long lasting problem of anomalous transport has been related, among other causes, to the onset of azimuthal plasma instabilities [22, 23] and their interaction with plasma turbulence [24, 25]. Anomalous electron transport across magnetic field lines arising due to instabilities with azimuthal characteristics is reported also in magnetrons [26] and Penning discharges [27].

Recent studies show that azimuthal oscillations are also present in the MN of EPTs [28, 29, 30]. Attempts to link these oscillations to different instabilities and plasma waves have been carried out, proposing them as causes of anomalous cross-field transport. Unfortunately, there is still no consensus on the origin, nature, nor the consequences of these oscillations, with some researchers pointing at a lower-hybrid drift instability leading to enhanced radially-outward transport [28], while others reporting a magnetosonic wave leading to inward transport [31]. Other studies discussing electron anomalous transport in MNs link it to the development of electrostatic turbulence induced by instabilities [32]. The existence of a region in MNs near the plasma edge where anomalous resistivity would dominate and interact with plasma turbulence was theorized in [33].

In addition to that, other studies also discuss the existence of low frequency ionization instabilities existing in EPTs [34, 35]. While some authors related the development of the observed oscillations to the existence of a current-free double layer inducing upstream flow of energized electrons from the expansion region into the source [34], others pointed at a predator-prey model to explain those [35]. Another study addressed the development of a similar oscillation in the same range of frequencies to an ion acoustic instability, successfully controlled by modulation of the injected radio-frequency signal [36]. Simulations of a MN expansion also related the existence of oscillations in the plume to a U-shaped double layer induced by radial charge separation, which would in turn excite ion Bernstein modes [37].

This paper focuses on the experimental characterization of oscillatory phenomena in the plasma of an ECRT device. The presented work proposes measurements acquired simultaneously with three plasma diagnostics: an array of 4 Langmuir probes (LPs), a curling probe (CP), and high-speed camera imaging to try to characterize the plasma fluctuations. Data at different operating points are analyzed, leading to the identification of different oscillation modes. Dispersion diagrams are reconstructed and non-linear power coupling among frequencies is explored by means of a bi-coherence estimate. The oscillations are captured with very good agreement also by the CP and the camera. The data from the CP allows to carefully follow the impact of the oscillations upon the plasma density, whereas the data from the camera is analyzed by means of Proper Orthogonal Decomposition (POD) to characterize the behavior of the light emitted by the plasma within the source. Possible explanations for the observed behaviors are explored.

The rest of the paper is structured as follows. Section II provides an overview of the experimental setup and the structure of the data. Experimental results are presented in Section III and discussed in Section IV. Finally, Section V draws the conclusions of this work.

II. Experimental setup

A. ECR thruster and vacuum facility

Data has been collected in the expanding plasma inside the magnetic nozzle of the 30 W ECR coaxial model developed at ONERA [7, 38, 39, 40]. This prototype employs a permanent magnet generating a strictly diverging magnetic field. Microwaves are injected at a frequency of 2.45 GHz at the rear of the thruster. The ECR condition is met a few millimeters downstream from the backplate in the thruster discharge chamber, where the magnetic field reaches 875 G. The device is typically fed with xenon at mass flowrates around 1 sccm (1 sccm $\simeq$ 0.1 mg/s for xenon), and microwave power at 2.45 GHz around 30 W. In the context of this study, the mass flowrate, the power deposited in the plasma, and the driving microwave frequency are varied from their typical values: between 1 and 2.2 sccm for the flowrate, between 13 and 33 W for the power deposited at the backplate, and between 2.00 and 2.60 GHz for the driving frequencies. The whole thruster is electrically floating and its potential naturally rises from a few tens to a few hundreds of volts with respect to the vacuum tank reference ground.

Measurements have been performed inside the B09 vacuum chamber, a cylindrical vessel of 0.8 m in diameter and 2 m long, at the ONERA premises in Palaiseau. The high vacuum pumping system consists of three turbomolecular pumps and one cryogenic pump, yielding a total pumping speed of 13 000 l/s for xenon, with a base pressure of about 3×10^{-7} mbar. In this work, the background pressure with the thruster firing is in the range $0.6 - 1.2 \times 10^{-5}$ mbar.

B. Plasma diagnostics

A set of three diagnostics has been used to characterize the plasma oscillations: an array of 4 Langmuir probes – developed at UC3M –, a microwave resonant curling probe – developed at ONERA –, and a high-speed camera – provided by ONERA. A single trigger signal enables to collect acquisitions synchronously. Additionally, the forward and reflected microwave power, alongside the thruster floating potential, are separately monitored. On the left of Figure 1, a sketch of the ECRT source and the magnetic nozzle is illustrated, alongside a visual representation of the whole experimental setup with the three diagnostics. The reference frame associated with the plasma source is the cylindrical coordinate system $(\hat{\boldsymbol{r}}, \hat{\boldsymbol{\theta}}, \hat{\boldsymbol{z}})$, whereas the probe system refers to a different, local frame $(\hat{\boldsymbol{\zeta}}, \hat{\boldsymbol{\alpha}}, \hat{\boldsymbol{\theta}})$. On the right of Figure 1, a photograph of the ECRT source and the probes is shown. The probe system, consisting of the LPs and the CP, can be moved within the 2D polar coordinate system $(\hat{\boldsymbol{\zeta}}, \hat{\boldsymbol{\alpha}})$ in the plasma plume using a motorized stage. Probes are mounted in a way to minimize possible perturbation of the setup on the plasma plume.

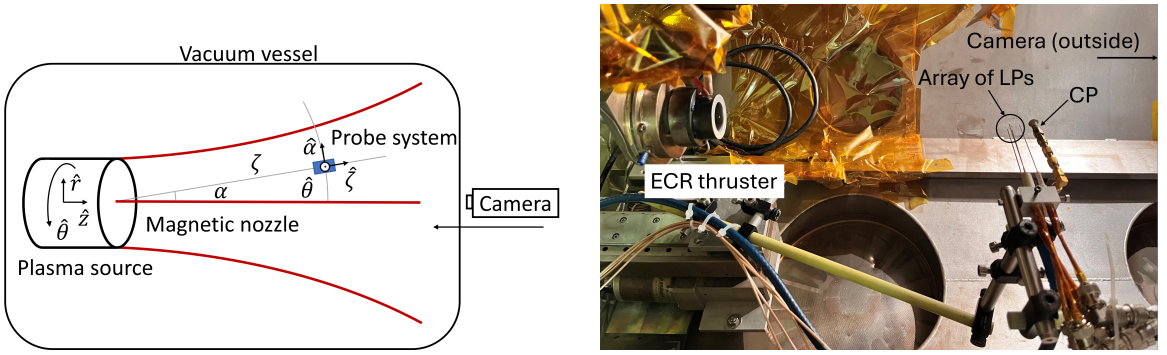

Figure 1: Left: Sketch of the ECRT source and its MN, alongside a visual representation of the whole experimental setup with the three diagnostics. The probe system, comprising the LP array and the CP, is immersed into the plasma and is represented with a blue rectangle, whereas the camera, placed outside of the vacuum vessel, to the right, faces the thruster exhaust and is focused on the thruster source. The cylindrical frame that refers to the plasma source is labeled $(\hat{\boldsymbol{r}}, \hat{\boldsymbol{\theta}}, \hat{\boldsymbol{z}})$. The spatial coordinates of the probe system in the 2D plane, instead, are based on a polar frame $(\hat{\boldsymbol{\zeta}}, \hat{\boldsymbol{\alpha}})$, with the origin fixed at the thruster exit plane. Right: photograph of the experimental setup, showing the array of LPs and the CP.

1. *Langmuir probes*

The array of LPs comprises four (identical) uncompensated Langmuir probes. The reference probe is placed in a central position, whereas the other 3 probes are fixed 10 mm apart from the reference one, each aligned along a different direction of $(\hat{\boldsymbol{\zeta}}, \hat{\boldsymbol{\alpha}}, \hat{\boldsymbol{\theta}})$. The LPs consist of an alumina body with a cylindrical tungsten tip measuring 0.25 mm in diameter and 4 mm in length. Probes are left electrically floating and are connected to the recording instrument through coaxial cables to minimize signal noise. The time variation of the floating potential is recorded with a Keysight Infiniium Mixed Signal Oscilloscope with 4 active channels, 4 GHz of bandwidth, 10 GSa/s of sampling rate, and 8 bits of vertical resolution. For each measurement point, 5 subsequent scans of 0.1 s of duration are collected. Each scan is then divided in 20 non-overlapping segments, yielding a total of 100 snapshots. This allows for increased statistical significance for averaging purposes.

In this work, the measurement of the floating potential of the LPs is used since (i) no power supply is required, (ii) problems related to low-pass filtering introduced by the presence of shunt resistors are minimized, and (iii) it introduces lower disturbances in the plasma as probes are not biased. Floating potential measurements have already been used as a proxy for plasma potential fluctuations under the assumption of constant electron temperature over the (expected) fluctuation time and space scales [16, 41, 42, 43].

The use of an array of 4 LPs allows to reconstruct an estimate of the real wavenumber vector in space, the *sample local wavenumber* $\boldsymbol{\kappa}(f) = (\kappa_\zeta, \kappa_\alpha, \kappa_\theta)$ – with $f = \omega/2\pi$ the linear frequency – obtained by means of the Two-Points Power Spectral Density (PSD2P) technique [44, 45]. The PSD2P consists in cross-correlating the signal of the reference LP, labeled as *LP 1*, which is placed at the front in a central position, with the signals of the other three probes, each one displaced along a different direction of the local frame $(\hat{\boldsymbol{\zeta}}, \hat{\boldsymbol{\alpha}}, \hat{\boldsymbol{\theta}})$ defined before. Namely, *LP 2* allows to obtain κ_ζ, *LP 3* is used to obtain κ_α, and *LP 4* yields κ_θ. The separation distance between each probe tip and the reference tip allows for the resolution of wavenumbers in the range $[-314, 314]$ rad/m. A schematic of the LP tips, with their labels and the local reference frame, is drawn in Figure 2. The direction $\hat{\boldsymbol{\zeta}}$, along which *LP 1* and *LP 2* are aligned, is meant to approximate at all times the parallel direction of the local magnetic field lines. The error for this approximation was found to be about 5 degrees at worst, at $\alpha = 30°$ and $\zeta = 130$ mm.

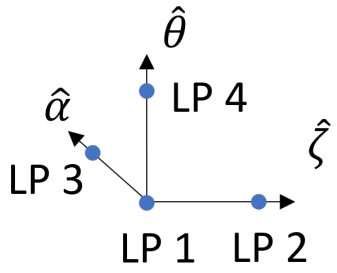

Figure 2: Schematic of the LP probe array, with the probe tips represented by blue dots and each probe labeled. The local reference frame $(\hat{\boldsymbol{\zeta}}, \hat{\boldsymbol{\alpha}}, \hat{\boldsymbol{\theta}})$ is also drawn alongside in black, for clarity. The probes *LP 1* and *LP 2* are aligned along the direction $\hat{\boldsymbol{\zeta}}$, which approximates at all times the parallel direction to the local magnetic field lines.

2. *Curling probe*

A curling probe is used to measure the electron density number ($N_{e,CP}$) inside the plasma. The CP is a microwave resonant probe consisting of a spiral resonator whose resonance frequency depends on the relative permittivity of the medium in which the probe is immersed. When the probe is immersed in a plasma, its resonance frequency (f_r) increases with respect to its reference value in vacuum (f_0). The electron density n_e can then be directly inferred from the frequency shift using [46] as

$$n_e = \frac{4\pi^2 m_e \epsilon_0}{e^2}(1+\alpha)(f_r^2 - f_0^2), \tag{1}$$

where α is a calibration coefficient, m_e the electron mass, e the elementary charge, and ϵ_0 the vacuum permittivity. The CP used in this work is called CP700: it has a spiral resonator length of 110 mm and a diameter of 10 mm. This CP has a vacuum resonance frequency around 880 MHz and it enables accurate measurements of plasma densities in the range $\simeq 8 \times 10^7 - 10^{10}$ cm^{-3}. We note that these values are given in terms of raw densities, i.e., the measured values that are affected by the plasma sheath effect. All density measurements presented here are corrected for the presence of the plasma sheath in front of the probe as detailed in [47]. Uncertainties on the raw measured density values are estimated following the method detailed in [46].

The resonance frequency of the probe is measured every 5 µs, enabling a 200 kHz sampling frequency of the electron density measurement. The CP is placed roughly 2.5 cm downstream the *LP 1* and is integral with the LP array, as can be seen in Figure 1. This position is chosen to minimize possible CP perturbations on the LP tips. The CP measuring surface is oriented in such a way to maximize the possibility to capture both azimuthal and axial density oscillations.

3. High-speed camera

The high-speed camera is positioned outside of the vacuum vessel and is imaging the thruster from the far-end window of the vacuum vessel, directly in front of the plasma source. The model is a Phantom v711, 12 bit resolution, running at 210 kHz with a 128 × 128 pixels image. The camera is set with a 107 mm fixed focal lens with a large opening of 2.8. The focal point is set at the thruster backplate, with the depth of field being a few centimeters. Due to the mounting of the camera, the light collected is averaged along the line of sight. However, experiments led with the camera imaging the thruster with a 45 and a 90 degrees angle, looking through lateral ports of the vacuum vessel, showed that the light produced by the plasma is very faint except in the first 1 cm downstream from the backplate, due to the very low pressure and very low plasma density in the thruster plume. The camera is therefore imaging only this first centimeter of plasma even when facing the thruster. No optical filter is used and the light in all the camera spectral sensitivity is contributing to the analyzed signal.

The acquired movies are analyzed over the first 1000 frames, granting a frequency resolution range of $[0.42, 105]$ kHz. Time-averaging of the entire movie is first computed, and the resulting image is subtracted to each frame in order to isolate light fluctuations. The obtained frames are then analyzed using POD [48, 49, 50, 51], previously employed to study plasma fluctuations in different plasma experiments [52, 53] and simulations [54]. This data-driven method allows to decompose a movie into its dominant spatial and temporal components (the POD modes), without any *a priori* assumption upon their shape. This only requires a small additional computational cost with respect to a Fourier decomposition. In the next sections, the computed modes contributing to the plasma fluctuations that will be displayed are only those with a relative energy content higher than 1.5 %. The camera diagnostic also allows to verify that shifting the probes position in the thruster plume does not modify the observed plasma fluctuations.

4. Thruster operating parameters

Additionally, three thruster parameters are recorded to monitor its operation: the forward microwave power (P_{fwd}), the reflected microwave power (P_{ref}), and the thruster floating potential (U_p). The forward power is estimated using a directional coupler placed on the forward power line coming from the microwave power generator with a RF power detector diode. The power reflected from the thruster, which is typically between 1 and 10% the forward power, is sent to a dedicated power line terminated by a 50 Ω load using a circulator. The reflected power is evaluated on this line using a second directional coupler and a RF power detector diode. The model of the two RF detectors is a JFW-50D-052 diode, with a cut-off frequency well above the oscillation frequencies measured in this work. The power deposited in the plasma is computed as $P_d = P_{fwd} - P_{ref}$. The thruster outer conductor floating potential is measured directly through a voltage divider bridge. These three variables are simultaneously recorded with an 8-bit oscilloscope at 20 MHz acquisition rate.

III. Results

This section presents the time-resolved measurements collected with the three diagnostics. In the following, the nominal operating condition of the thruster is to be intended for $P_d = 30$ W of power deposited

into the plasma, an injected mass flowrate of $\dot{m} = 1.4$ sccm, and a microwave driving frequency equal to $f_{mw} = 2.45$ GHz.

It is worth to note that time-averaged measurements of the plasma density, the electron temperature, and the plasma potential have been collected with the LPs operated in sweeping mode and with the CP at the same positions of the time-resolved measurements. A good agreement has been found with previous measurements on this thruster prototype [55, 56]. Those measurements are not shown here.

A. Thruster parameters

Figure 3 shows the power spectral density (PSD) of the signals recorded during the experimental campaign at (a) 1.4 sccm and (b) 1 sccm. The probe measurements are collected at $\zeta = 70$ mm and $\alpha = 0°$.

At $\dot{m} = 1.4$ sccm, all signals show a visible low-frequency peak around 9 kHz, as seen in Figure 3-(a). In addition, electron density, LP floating potential, and thruster floating potential display a second, higher-frequency peak at around 60 kHz. This indicates that two distinct plasma oscillations exist in the plume, which will be referred to in the remaining of the paper *low-frequency* and *higher-frequency* oscillations, respectively. In particular, a very good agreement in the value of the oscillation frequency and the PSD shape is observed among $N_{e,CP}$, U_p, and $V_{f,LP}$. The peak-to-peak amplitude of the oscillations is summarized in Table 1 for all signals. The relative amplitude of the electron density and the reflected power is comparable (22% and 20%, respectively), as is that of the thruster potential and the LP floating potential (10% and 8%, respectively). On the other hand, the relative amplitude of the forward power signal at 9 kHz is very small, with values well below 1%.

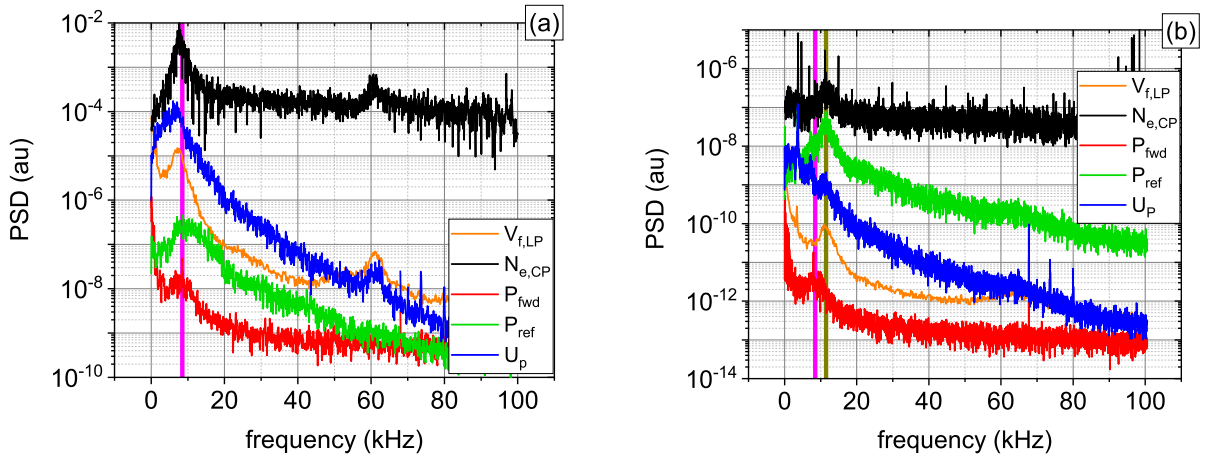

Figure 3: PSD of the 5 signals recorded during the measurement campaign: LP floating potential ($V_{f,LP}$, orange line), electron density measured with the CP ($N_{e,CP}$, black line), forward power to the thruster (P_{fwd}, red line), reflected power from the thruster (P_{ref}, green line), and thruster floating potential (U_p, blue line). All quantities are plotted in arbitrary units on the y-axis to aid visualization and avoid line overlapping. (a) 1.4 sccm, (b) 1 sccm.

Table 1: Peak-to-peak oscillation amplitude at 9 kHz of the quantities shown in Figure 3-(a) at 1.4 sccm. Each value is normalized by the respective mean value of the recorded time series.

measured quantity, A	pk-pk amplitude $\Delta A/\bar{A}$
P_{fwd}	$\leq 1\%$
P_{ref}	$\simeq 20\%$
U_p	$\simeq 10\%$
$N_{e,CP}$	$\simeq 22\%$
$V_{f,LP}$	$\simeq 8\%$

In order to answer the question about whether the observed low-frequency plasma oscillation at approxi-

mately 9 kHz is due to the forward power (i.e., it is introduced by the power supply) or it is induced by the plasma, we analyze their relationship more in detail.

First, forward and reflected power without plasma ignition were recorded. In such case, the microwave power reaches the coaxial thruster chamber: a small part is radiated from the thruster, while the remaining power is reflected back to the line and dissipated through a 50 Ω load. Results indeed indicate the existence of some power concentration at around 9 kHz in the PSD of the P_{fwd} signal. This frequency is close to the values of the low-frequency plasma oscillation obtained for 1.4 sccm (see the pink vertical line in Figure 3-(a)).

On the other hand, when different operating conditions are inspected, the low-frequency peak observed for the plasma related quantities is not at 9 kHz, as is shown for instance in Figure 3-(b) for $\dot{m} = 1$ sccm. In this case, the low-frequency oscillation peaks in correspondence to the gold vertical line, located at $\simeq 12$ kHz, whereas the peak of P_{fwd} remains at 9 kHz, highlighted once again by the pink vertical line. The dependency of the fundamental frequency of the low-frequency oscillation on the thruster operating conditions points in the direction of a plasma-driven oscillation. It appears however that the power supply employed in this work introduces a $\simeq 9$ kHz fluctuation of the input power due to ripple. At a flowrate of 1.4 sccm, the fundamental frequency of the low-frequency plasma-driven oscillation approaches 9 kHz, and a resonance may occur. Indeed, the largest amplitude of the low-frequency mode is experimentally observed for 1.4 sccm, which is the reason why this operating condition was taken as nominal throughout this study.

In conclusion, it can be assumed, through experimental evidence, that the low-frequency oscillation observed is not induced by the power supply, but is rather plasma-driven. Nevertheless, it is likely that the oscillation interacts with the 9 kHz ripple of the power supply when at 1.4 sccm, and that the two resonate for this condition. Further measurements with different power supplies will be performed to assess the validity of this hypothesis.

B. Langmuir probes

Langmuir probe results are shown in Figure 4, where the PSD spectrum of the signal collected by the *LP 1* is shown at different angular positions α and at two different axial positions: (a) $\zeta = 70$ mm and (b) $\zeta = 130$ mm, for the nominal operating condition. Firstly, results show the predominant low-frequency oscillation around 9 kHz, consistently visible for all investigated positions. The higher-frequency oscillation is also detected falling in the 60–70 kHz range, generally possessing lower magnitudes with respect to the low-frequency one. Comparison of the spectra shows how both the strength and the dominant frequency of the 9 kHz $V_{f,LP}$ fluctuation remain roughly unaffected by the investigated spatial position. On the contrary, whilst the 60–70 kHz oscillation appears to consistently fall within the same range of frequencies, its intensity seems to have a dependency upon the angular position, getting slightly stronger for higher values of the coordinate α, but being generally visible everywhere.

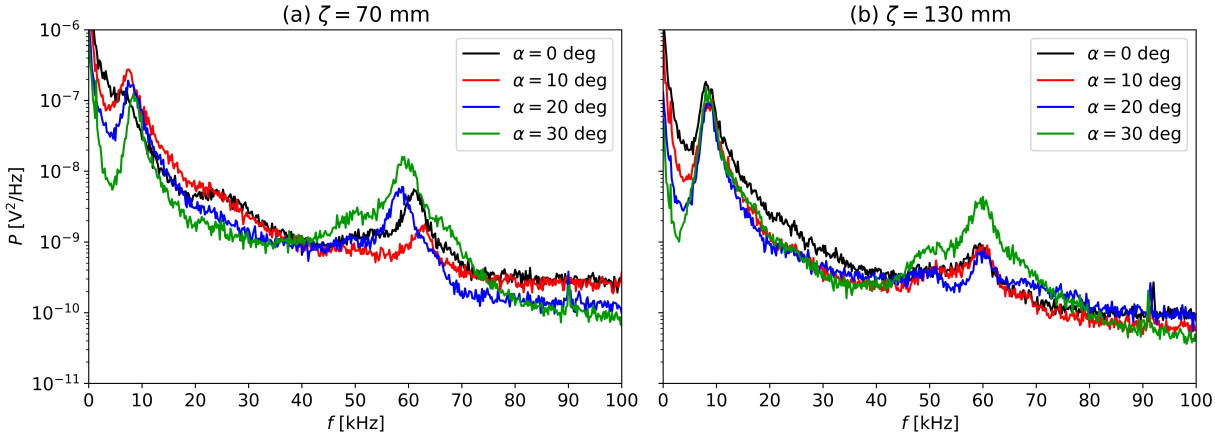

Figure 4: PSD of the *LP 1* signal collected at different angular positions, at (a) $\zeta = 70$ mm and (b) $\zeta = 130$ mm. For both (a) and (b), $\dot{m} = 1.4$ sccm, $P_d = 30$ W.

Figure 5 shows the PSD of the *LP 1* signal when varying the thruster operating conditions, in terms of (a) mass flowrate, (b) power deposited in the plasma, and (c) microwave driving frequency. The LP array

is located at $\zeta = 130$ mm and $\alpha = 20°$. Additionally, Figure 5-(d) shows the PSD spectra obtained from measurements collected on different days of testing to assess repeatability. The measurements in (d) are taken along the centreline, namely at $\zeta = 130$ mm and $\alpha = 0°$.

As shown in Figure 5-(a), the low-frequency oscillation is clearly visible with a well defined peak at 1 sccm, around 12 kHz, and at 1.4 sccm, around 9 kHz, for which the amplitude is highest. When the flowrate is increased beyond 1.4 sccm, the amplitude of this oscillation is seen to gradually decrease. More precisely, by means of previous acquisitions that will not be shown in this paper, this oscillation was detected from $\dot{m} = 0.8$ sccm up to roughly 1.6 sccm, always centered between 5 and 12 kHz. For $\dot{m} \geq 2$ sccm, the low-frequency oscillation tends to disappear and only a small plateau can be seen slightly below 10 kHz. The higher-frequency oscillation is generally visible at around 60, 45, 25 kHz when increasing the flowrate from 1 to 2.2 sccm, with varying amplitude.

Variations of the input power P_d, as displayed in Figure 5-(b), have a much milder effect on the observed dynamics. The dominant frequency of the low-frequency oscillation is slightly increased to 11 kHz when decreasing the power to 13 W. Conversely, for this same value of P_d, the amplitude of the high-frequency oscillation is reduced by around a third compared to the 30 W power level. For $P_d = 33$ W, the low-frequency oscillation is not changed, whereas the higher-frequency one shows a small shift of its dominant frequency.

Variations of the input microwave frequency appear to have a major impact on the intensity of both the low and higher-frequency oscillations, as shown in Figure 5-(c). Specifically, reducing the microwave frequency to 2.00 GHz does not massively change the frequency of the main low-frequency peak, which remains roughly in proximity of 9 kHz, but it increases its amplitude by at least two orders of magnitude. Five harmonics of the main frequency are also observed. The higher-frequency oscillation instead disappears entirely for this condition. On the other hand, increasing f_{mw} to 2.60 GHz has the opposite effect, remarkably damping the low-frequency oscillation in magnitude. The amplitude of the higher-frequency oscillation is significantly enhanced by approximately two orders of magnitude compared to the nominal 2.45 GHz case.

Finally, measurement consistency is assessed in Figure 5-(d), where the PSD extracted from the signals collected by the *LP 1* on different days of testing is illustrated. The operating condition is the nominal one, with the LP array located at $\zeta = 130$ mm and $\alpha = 0°$. PSD spectra show very good repeatability: the low and higher-frequency oscillations are visible at the same frequencies (at around 9 and 60 kHz, respectively) and with the same magnitude.

Application of the PSD2P technique allows for the computation of the experimental dispersion diagrams $\kappa - f$, providing further insight into the observed low and higher-frequency dynamics. These dispersion diagrams are shown in Figure 6 for all three spatial directions, with the LP array located at $\zeta = 130$ mm and $\alpha = 30°$, a position for which both the low and higher-frequency oscillations show large amplitudes, and for the nominal operating condition. The colorbar reports the value of the *magnitude-squared coherence (MSC)* $r(f)$ [57], which is computed along each direction. The dispersion diagrams display very high values of coherence in proximity to the characteristic frequencies at which the two main oscillations take place, namely around $f = 9$ kHz and 60 kHz, suggesting that a wave is present. Around those frequencies, where the MSC peaks, the values of the sample local wavenumbers are small. Only the dispersion diagrams along the radial direction $\hat{\boldsymbol{\alpha}}$ and the azimuthal direction $\hat{\boldsymbol{\theta}}$ show a faint right-wise trend for frequencies roughly between 10 and 50 kHz, with the radial trend being slightly more pronounced. Those trends, however, are interrupted right before $\simeq 60$ kHz, where the MSC increases, and κ_α and κ_θ move back to values near the centre of the dispersion plots. Other spatial positions – not reported here for brevity – show comparable behaviors, with generally small values of the local wavenumbers for large values of the coherence.

The signal collected by the *LP 1* is further processed by means of the *bi-coherence analysis* [58]. The bi-coherence analysis provides with a normalized value $b(f_1, f_2)$ between 0 and 1, which estimates the quadratic non-linear interaction intrinsic to the data between a pair of modes at frequencies f_1 and f_2 and a mode at the sum-frequency $f_1 + f_2$. Within the scope of this work, the objective is to use this technique to identify pairs of interacting frequencies (namely, f_1 and f_2) in the context of three-wave coupling.

Figure 7-(a) displays the results obtained through application of the bi-coherence analysis for the nominal operating condition, the same as in Figure 6. For this case, the extracted values of b are small overall, indicating a generally low level of non-linear interaction. The highest contribution, around $\simeq 0.15$, is found at $(f_1, f_2) \simeq (60, 10)$ kHz, displaying a central region of quasi-null bi-coherence and two sideband regions with higher b. Sideband structures are typical of signal modulation, which is in fact a type of quadratic non-linear interaction. Such sideband structures are also visible for some positions and/or operating conditions in the PSD spectra of Figures 4 and 5, at the two sides of the fundamental frequency of the higher-frequency

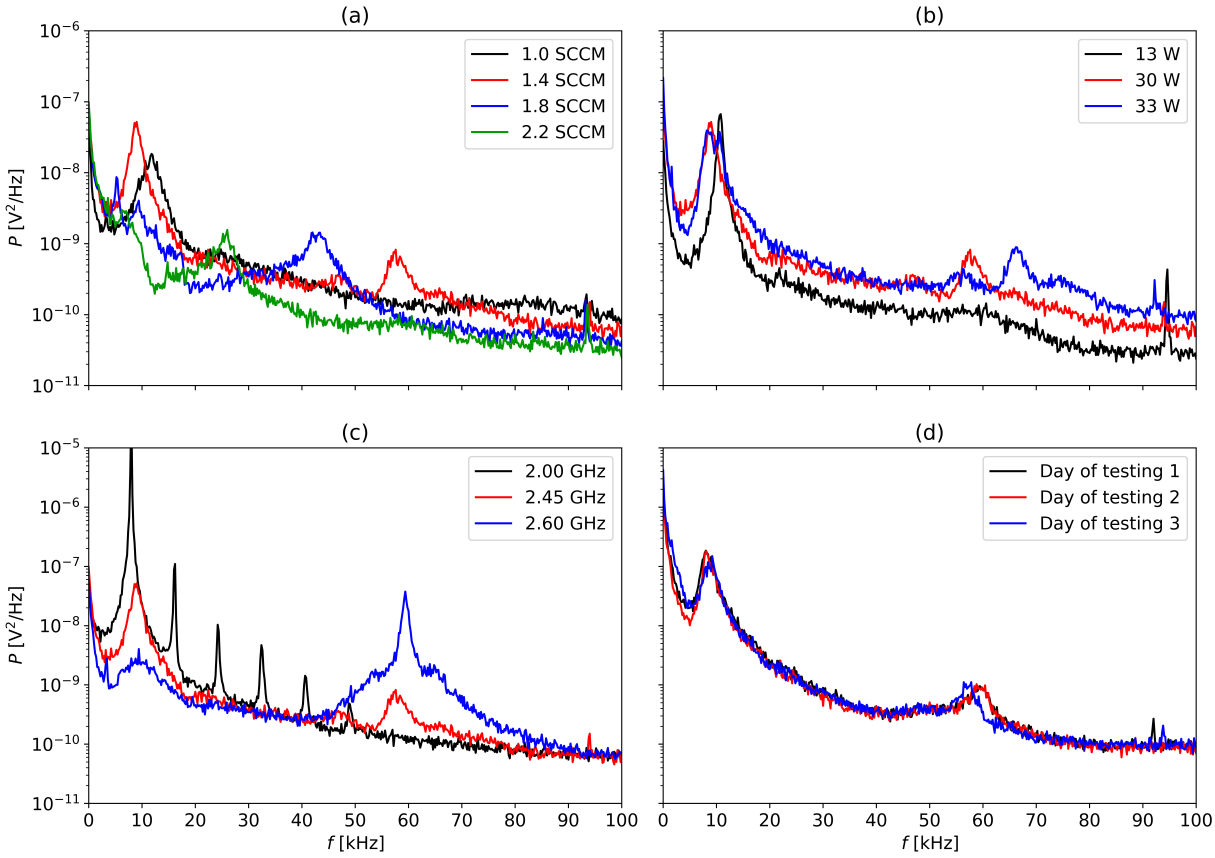

Figure 5: PSD spectra of the signal collected by the *LP 1* for variations, with respect to the nominal operating condition, of (a) mass flowrate, (b) power deposited in the plasma, and (c) driving frequency. All the scans in (a)–(c) are obtained at the same spatial position given by $\zeta = 130$ mm and $\alpha = 20°$. Lastly, (d) displays the repeatability of the measurements, for the nominal operating condition, by means of independent acquisitions performed during different days of testing, at $\zeta = 130$ mm and $\alpha = 0°$.

oscillation. This implies that the higher-frequency oscillation is undergoing modulation on behalf of the low-frequency one.

A much different scenario is recovered for the case depicted in Figure 7-(b), for which the overall values of bi-coherence are much higher. The inspected spatial position is $\zeta = 130$ mm and $\alpha = 20°$, while the operating condition is $P_d = 30$ W, $\dot{m} = 1.4$ sccm, and $f_{mw} = 2.00$ GHz. This is the case showing strong harmonic generation for the low-frequency oscillation, as displayed in Figure 5-(c). This is confirmed by the strong, localized non-linear interaction detected at values of f_1 and f_2 corresponding to harmonics of the fundamental frequency of the low-frequency oscillation. This implies that the majority of their energy can be explained solely in terms of harmonic generation from the fundamental frequency. Again, this is in contrast with the previous case, where the lower magnitudes of the bi-coherence hinted at weak couplings or energy transfer explained by other processes or plasma instabilities.

C. Curling probe

Figure 8 shows the comparison of the PSD spectra of the CP electron density (black line) and the LP floating potential (orange line) recorded at $\zeta = 70$ mm and (a) $\alpha = 0°$ and (b) $\alpha = 30°$, at nominal operating condition. Globally, a good agreement is observed in the values of the low and higher-frequency oscillations (around 9 and 60 kHz) for the CP electron density and LP floating potential signals, especially on the axis ($\alpha = 0°$, Figure 8-(a)). At $\alpha = 0°$, the low-frequency magnitude is around 50× above the floor level, whereas the higher-frequency magnitude is around 4× above the floor level. Away from the axis, at $\alpha = 30°$ (see

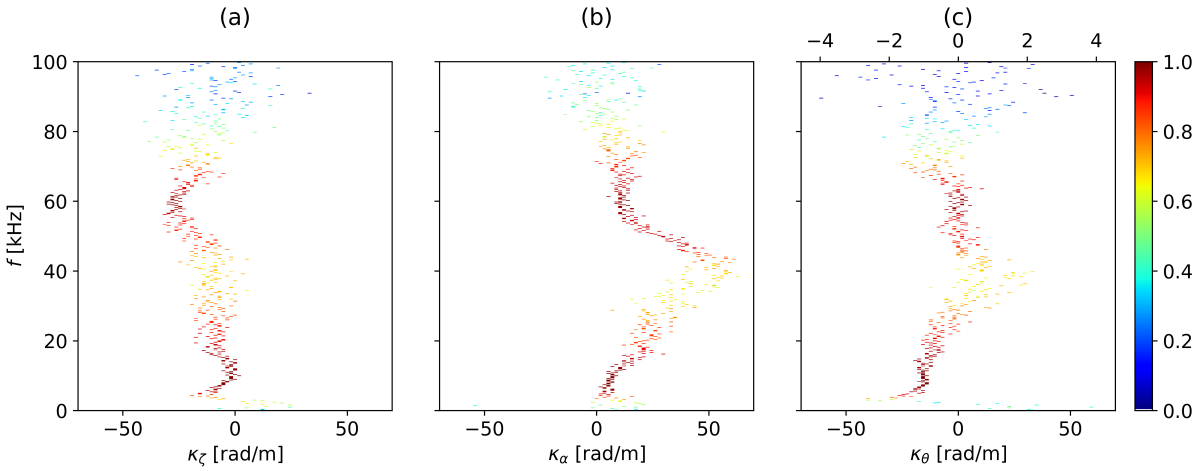

Figure 6: Experimental dispersion diagrams for the nominal operating condition, at $\zeta = 130$ mm and $\alpha = 30°$, obtained by means of the PSD2P technique. The three sample local wavenumber components $\kappa(f)$ are displayed, namely along the directions (a) $\hat{\boldsymbol{\zeta}}$, (b) $\hat{\boldsymbol{\alpha}}$, and (c) $\hat{\boldsymbol{\theta}}$. The colorbar represents the corresponding values of the MSC $r(f)$. An additional x-axis is drawn on top of panel (c) to report the normalized m modes. Note that the sampled wavenumbers span $[-314, 314]$ rad/m, but the plots are zoomed in the regions of interest.

Figure 8-(b)), the low-frequency peak of the PSD has a lower magnitude (only 8× above the floor level *vs.* $\simeq 50\times$ above the floor level for the $\alpha = 0°$ case). Moreover, the higher-frequency peak is not detected with the density measurement performed with the CP. This is most likely due to the fact that the amplitude of the 60 kHz density oscillation at $\alpha = 30°$ is below the measurable range of the CP utilized in this work.

At $\alpha = 0°$, the average electron density is $\simeq 8 \times 10^9$ cm^{-3} and the peak-to-peak amplitude of the low-frequency oscillation is $\simeq 1.3 \times 10^9$ cm^{-3}, yielding a ratio $\Delta N_{e,pk-pk}/\bar{N}_e \simeq 17\%$. When moving out of the centreline, at $\alpha = 30°$, the average electron density and the peak-to-peak amplitude of the low-frequency oscillation are $\simeq 1.5 \times 10^9$ cm^{-3} and 10^9 cm^{-3}, respectively, which corresponds to $\Delta N_{e,pk-pk}/\bar{N}_e \simeq 70\%$. Assuming that the magnitude of the higher-frequency oscillation is consistently approximately 10× lower than that of the low-frequency one, as for the $\alpha = 0°$ case, then the (raw measured density) amplitude of the higher-frequency oscillation would be $\simeq 10^7$ cm^{-3}, well below the measurable density range of the probe.

Access to direct measurements of the electron density mean value and fluctuations amplitude is of particular interest when performing theoretical predictions of classical and anomalous transport coefficients [59]. For example, the relative density amplitude $\Delta N_e/\bar{N}_e$ can be used to estimate an effective electron resistivity related to cross-field particle transport.

Figure 9 shows (a) the absolute and (b) the relative peak-to-peak amplitude of the density fluctuations in time when moving farther away from the thruster for two angular positions, $\alpha = 0°$ and $\alpha = 30°$, at nominal operating condition. The absolute density amplitude, shown in Figure 9-(a), globally decreases with distance to the thruster for the two angular positions. Moreover, for $\zeta < 12$ cm it is larger on the axis than at $\alpha = 30°$. For $\zeta > 12$ cm the amplitude on the axis is comparable to that away from the axis. The relative density amplitude, shown in Figure 9-(b), is much larger at $\alpha = 30°$ than at $\alpha = 0°$ for all distances, with values around 70% and 20% at $\alpha = 30°$ and $\alpha = 0°$, respectively. In addition, the relative amplitude decreases from 80% to 60% with the distance to the thruster in the $\alpha = 30°$ case, whereas at $\alpha = 0°$ it slightly increases from 20% to 25%.

Last, we show the influence of the microwave driving frequency on the amplitude and frequency values of the low-frequency density oscillation in Table 2. Globally, the amplitude of the density oscillations decrease when increasing the driving frequency value. When the microwave frequency is decreased from the nominal value (2450 MHz) to 2000 MHz, therefore moving the ECR region downstream inside the thruster source (see Figure 12), the absolute amplitude of the oscillation increases by 1.6× and the relative one by almost 4×. When the driving frequency is increased to 2600 MHz, corresponding to an ECR region much closer to the thruster backwall, as shown in Figure 12, the absolute amplitude decreases by 1.6× (which is the same

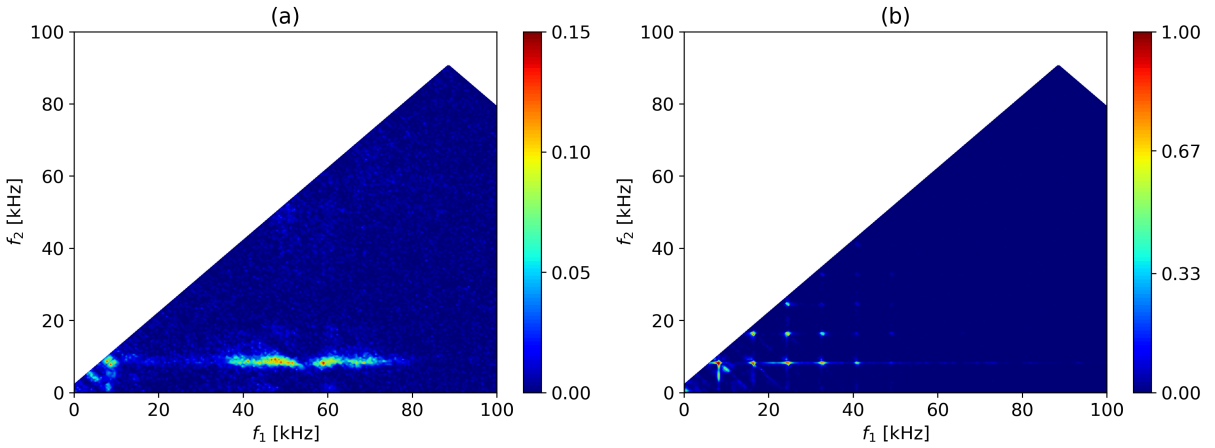

Figure 7: Bi-coherence diagrams for the signal collected by the *LP 1* in two different scenarios, namely for (a) $\zeta = 130$ mm, $\alpha = 30°$, $\dot{m} = 1.4$ sccm, $P_d = 30$ W, $f_{mw} = 2.45$ GHz, and for (b) $\zeta = 130$ mm, $\alpha = 20°$, $\dot{m} = 1.4$ sccm, $P_d = 30$ W, $f_{mw} = 2.00$ GHz. Note that the upper limits of the two colorbars are different.

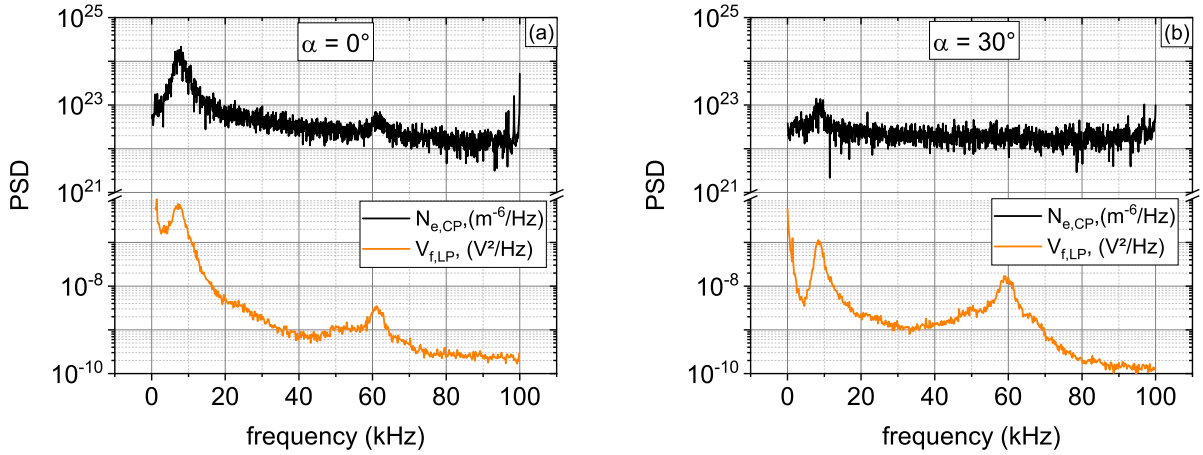

Figure 8: Computed PSD of the electron density measured with the CP (black line) and the LP floating potential (orange line) at $\zeta = 70$ mm and (a) $\alpha = 0°$ and (b) $\alpha = 30°$.

amount by which it increases when moving to the 2000 MHz case) and the relative one is decreased by less than 2×.

D. High-Speed Camera

Firstly, the camera is used to verify that the probe system, comprised of the array of LPs and the CP, does not affect the measured plasma fluctuations. The camera measurements are performed both with the probes outside of the plasma, moving the mechanical arm on the far side of the plume, and with the probes immersed in the plasma, for each position of the probe setup. For fixed operating conditions, the plasma fluctuations collected by the camera are observed to be unaffected while the position of the set of probes is varied. This serves the purpose of verifying that the array of probes does not affect the visible plasma fluctuations, validating the fact that the evolution of the fluctuations observed with the probes can be attributed to local plasma behaviour and not to modification of the thruster operation.

Secondly, the movies collecting fluctuations of the light emitted by the plasma at the nominal operating condition are analyzed, in order to assess their geometrical shape. The first four dominant spatial modes obtained by POD analysis, labeled u_0 to u_3, are displayed with their relative energy contributions, from

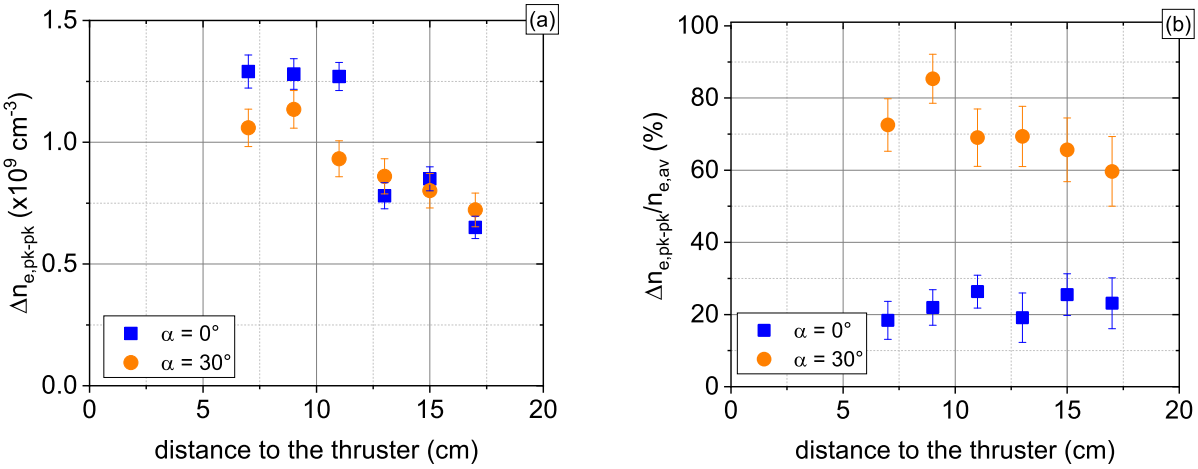

Figure 9: (a) Density oscillation absolute amplitude along the thruster plume on the axis (blue scatter points) and off the axis (orange scatter points), and (b) density oscillation amplitude normalized by the average density at various axial positions.

Table 2: Amplitude of the density oscillation for the three driving microwave frequencies analyzed in this study (2450 MHz is the nominal case). Data has been collected at $\zeta = 130$ mm and $\alpha = 0°$.

Driving frequency [MHz]	$\Delta N_{e,pk-pk}$ [$\times 10^9$ cm^{-3}]	$\Delta N_{e,pk-pk}/\bar{N}_e$ [%]
2000	1.3 ± 0.07	72 ± 5
2450	0.8 ± 0.05	19 ± 2
2600	0.5 ± 0.05	11 ± 1

77.4% to 2.5%, in Figure 10. The first POD mode is almost homogeneous over the thruster diameter and is strongly dominating the other three modes that are not spatially homogeneous. The dominant u_0 mode can be described as a global $m = 0$ mode. The POD modes u_1, u_2, and u_3 present both a radial and an azimuthal inhomogeneity and may be attributed to azimuthal $m = \pm 1$ modes.

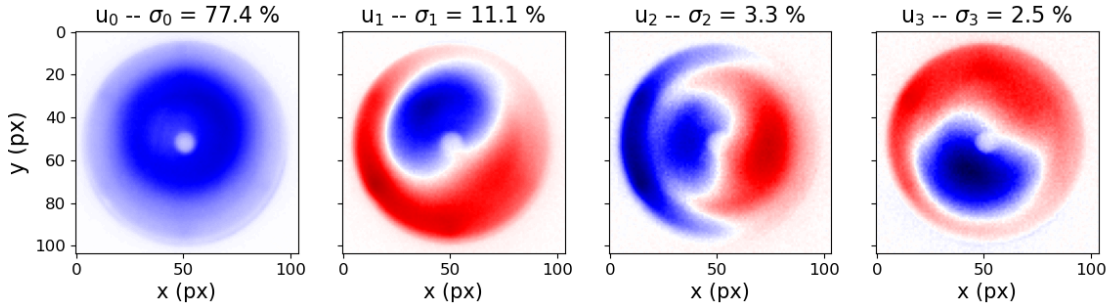

Figure 10: Dominant spatial modes obtained by means of the POD technique applied to the signal of the high-speed camera for the ECR thruster operated at nominal condition.

Furthermore, the PSD of the temporal evolution of the four dominant POD modes is computed. Results are presented in Figure 11, demonstrating that the major spectral contributions captured by both the LPs and the CP can also be found with POD analysis. Additionally, this plot confirms the prevalence of mode u_0, showing a peak at 9 kHz that is one order of magnitude larger than the second largest peak reached by the mode u_1. The peak captured around 60 kHz by the LPs and the CP is also present with lower magnitudes on the signals of the modes u_0 and u_3, but is not detected by modes u_1 and u_2.

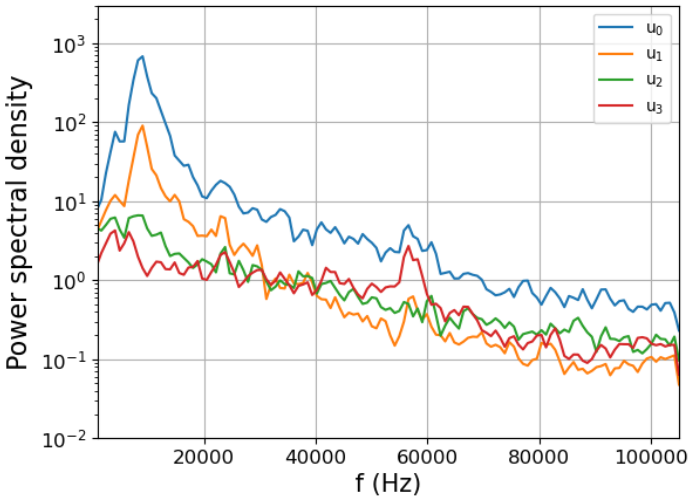

Figure 11: PSD of the temporal evolution of the four dominant modes obtained with the POD technique applied to the high-speed camera signal for the ECR thruster operated at 30 W and 1.4 sccm.

IV. Discussion

Globally, results from the three independent diagnostics, namely an array of LPs, a CP, and a high-speed camera, evidence the presence of two plasma oscillations, at around 9 kHz and 60 kHz, in the plume and in the plasma source of the investigated ECR thruster prototype. In the following, we will discuss the two oscillations separately.

A. The low-frequency oscillation

The low-frequency oscillation was found to fall in a range of frequencies between 5 and 12 kHz, with an intensity mostly affected by changes in the mass flowrate and the microwave driving frequency (see Figure 5-(a) and (c)). POD analysis of the light captured by the camera suggested that this oscillation carries most of the energy, with a predominant $m = 0$ global mode structure (Figure 10). Indeed, the experimental dispersion diagrams shown in Figure 6 displayed a small propagation in space in correspondence to its fundamental frequency. In this case, the electron density was seen to oscillate with a peak to peak amplitude amounting to a significant fraction of its average value.

These observations suggest that this oscillation may be related to an ionization type of dynamics. Ionization processes have already been shown to induce low-frequency plasma oscillations in other electric propulsion devices, such as in Hall effect thrusters, in which they are often referred to as *breathing oscillations* [60, 61], in magnetic nozzle thrusters [34, 36], and more particularly in ECR thrusters [35]. In addition, this kind of oscillations has also been observed in other plasma sources, such as in ECR sources [21] and in hollow cathodes [62, 63]. Breathing oscillations are often found to strongly modulate the plasma dynamics and are generally observed at multiple positions within the plume [64, 65]. Furthermore, they tend to have a global behavior, with little to no propagation [66, 67], and their characteristic frequencies fall in the 1–50 kHz range [68].

A simple model describing breathing oscillations is the predator-prey model, originally developed by Fife *et al.* [67] in the context of Hall thrusters, and later revisited in refs. [69, 70]. According to its simplest formulation, it relies on a global analysis of 0D continuity equations for ions and neutrals, localized within a confined ionization region of length L. The solution of this system of equations is a standing wave with an oscillating frequency, representing the hybrid residence time of ions and neutrals within the chamber, defined as

$$\omega = 2\pi f = \frac{\sqrt{v_n v_i}}{L}, \tag{2}$$

where v_i and v_n are the ion and neutral characteristic velocities in the ionization region, respectively. Neutrals are assumed to be at room temperature, yielding $v_n \approx 138$ m/s in the case of xenon. The ion velocity is inferred from previous measurements on a similar thruster prototype [55]: at 10 mm from the backplate and for different values of the mass flowrate, typical values of v_i are between 1700 and 2800 m/s. If the characteristic ionization length is taken equal to $L = 10$ mm [56], the theory predicts frequencies falling between 7 and 10 kHz, which are close to the values measured in this work for the low-frequency oscillation.

The variation of the forward power to the thruster does not seem to induce major effects other than slightly shifting its fundamental frequency. On the other hand, the variation of the driving microwave frequency impacts the amplitude of the low-frequency oscillation by several orders of magnitude, as displayed in Figure 5-(c) and reported in Table 2. One preliminary explanation for this strong shift in amplitude can be attributed to the fact that the ECR region moves along the chamber while the driving microwave frequency changes. A visual representation of the position of the three ECR regions for the three driving frequencies tested in this work is given in Figure 12. The position of the ECR region can potentially have a non-negligible impact upon the ionization process and ultimately affect the corresponding ionization efficiency. This, in turn, may further support the theory attributing the low-frequency oscillation to an ionization-related process.

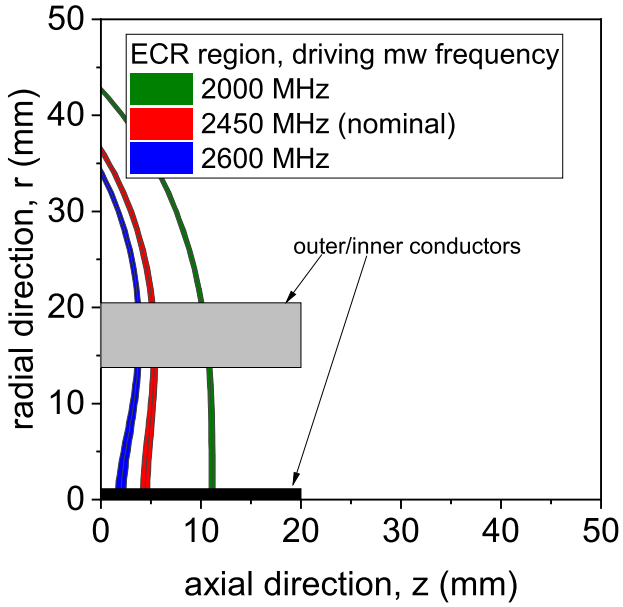

Figure 12: ECR regions for the three driving microwave frequencies tested in this work: 2000, 2450 (nominal case), and 2600 MHz.

B. The higher-frequency oscillation

For what concerns the higher-frequency oscillation, it was shown in Section III-B how its intensity seemed to be slightly enhanced when moving towards the edge of the plume, but being this oscillation also detectable along the axis (see Figure 4) and in the thruster source (through the high-speed camera measurements, see Figure 11). Its fundamental frequency showed an important dependency on the injected mass flowrate, gradually moving to lower frequencies when increasing $\dot{m}$ (see Figure 5-(a)). The spatial structure identified by means of the PSD2P technique involved generally small values of the wavenumbers around 60 kHz, with some trends, though faint, along the radial and azimuthal directions. POD modes with noticeable energetic contributions at 60 kHz also exhibited some azimuthal and/or radial structure, but proper isolation of this oscillation was prevented by mode interplay. Finally, bi-coherence analysis underlined weak non-linear interaction of the higher-frequency oscillation with the low-frequency oscillation in the form of signal modulation.

Several recent studies report the existence of oscillations in the peripheral region of various devices employing MNs. Notably, evidence of broadband oscillations with azimuthal propagation was reported by Hepner *et al.* [28] in an ECRT device with a design similar to the one employed in this study. The oscillation

was attributed to a Lower-Hybrid Drift Instability, a collisionless, kinetic type of instability that takes place in the lower-hybrid frequency regime. Takahashi *et al.* [29] also reported azimuthally rotating oscillations in the periphery of a MN, with typical frequencies in the 40–50 kHz range, this time employing a Helicon Plasma Thruster. The oscillation was attributed to a magnetosonic wave, corresponding to a compressional Alfvén wave. Additional evidence of broadband azimuthal oscillations developing in the periphery of the plume of a Helicon Plasma Thruster, falling around 50 kHz, was reported in [30]. The oscillation was seen to possess features that are typical of a lower-hybrid type of wave. The characteristic frequencies reported in those studies are close to the characteristic frequency of the higher-frequency oscillation found in this work, typically around 60 kHz. The lower-hybrid frequency, instead, is typically found to fall a few times above that value, roughly between 200 and 300 kHz.

V. Conclusions

In this work, plasma oscillations in the MN of a coaxial ECRT device were experimentally detected and characterized. The experimental acquisitions were collected by means of three different diagnostics: an array of LPs, a CP, and a high-speed camera. All diagnostics collected data simultaneously.

The results obtained independently with the three diagnostics showed good agreement. The experimental findings allowed to detect two separate oscillating phenomena, one at low frequencies, typically below 15 kHz, and a second one taking place around 60 kHz. The dependency of these two oscillations on changes of the thruster operating condition and the probe position within the plasma plume was investigated.

The low-frequency oscillation was observed almost everywhere in the plume with similar intensity, displaying a fundamental frequency that, depending on the operating condition, always fell between 5–12 kHz. The oscillation was seen to possess a predominant $m = 0, -1$ azimuthal structure, and electron density was seen to fluctuate accordingly with a significant fraction of its average value. The higher-frequency oscillation was also seen almost everywhere, with a slight dependency on the inspected spatial position. Changes in the power deposited into the plasma did not affect, in a major fashion, the features of the observed oscillations. Conversely, variations of the mass flowrate and the microwave driving frequency did affect their strength and fundamental frequency in a remarkable way.

The possibility that the low-frequency oscillation be induced by an ionization instability was suggested and a plausible agreement of the physics observed experimentally with expected characteristic frequencies. Conversely, the higher-frequency oscillation was seen to fall in a range of frequencies that resembles existing evidence of various phenomena observed in other or similar devices [28, 29, 30]. Further analysis of the data and additional testing will be performed in order to confirm the validity of the formulated hypotheses and advance the understanding of the two detected oscillations.

Acknowledgments

This work has received funding from the European Research Council (ERC) under the European Union's Horizon 2020 research and innovation programme (Starting Grant ZARATHUSTRA, grant agreement No 950466).

References

[1] Navarro-Cavallé, J., Wijnen, M., Fajardo, P., Ahedo, E., Gómez, V., Giménez, A., and Ruiz, M., "Development and Characterization of the Helicon Plasma Thruster Prototype HPT05M," 36^{th} International Electric Propulsion Conference, No. IEPC-2019-596, Electric Rocket Propulsion Society, Vienna, Austria, 2019.

[2] Packan, D., Elias, P.-Q., Jarrige, J., Vialis, T., Correyero, S., Peterschmitt, S., Porto-Hernandez, J., Merino, M., Sánchez-Villar, A., Ahedo, E., Peyresoubes, G., Thorinius, A., Denis, S., Holste, K., Klar, P., Scharmann, S., Zorn, J., Bekemans, M., Scalais, T., Bourguignon, E., Zurbach, S., Azais, P., Habbassi, I., Mares, M., and Hoque, A., "H2020 MINOTOR: Magnetic nozzle electron cyclotron resonance thruster," 36^{th} International Electric Propulsion Conference, No. IEPC-2019-875, Electric Rocket Propulsion Society, Vienna, Austria, 2019.

[3] Glover, T., Chang, D., Franklin, R., Squire, J., Jacobson, V., Chavers, D., Carter, M., El-Genk, M., and Bragg, M., "Principal VASIMR results and present objectives," AIP Conference Proceedings, Vol. 746, AIP Publishing, Melville, NY, 2005, pp. 976–982.

[4] Jarrige, J., Elias, P., Cannat, F., and Packan, D., "Performance comparison of an ECR plasma thruster using argon and xenon as propellant gas," 33rd International Electric Propulsion Conference, Paper 2013-420, Electric Rocket Propulsion Society, Fairview Park, OH, Washington D.C., October 7-10, 2013.

[5] Peterschmitt, S., Development of a stable and efficient electron cyclotron resonance thruster with magnetic nozzle, Ph.D. thesis, Institut Polytechnique de Paris, 2020.

[6] Désangles, V., Packan, D., Jarrige, J., Peterschmitt, S., Dietz, P., Scharmann, S., Holste, K., and Klar, P., "ECRA thruster advances, 30W and 200W prototypes latest performances," Journal of Electric Propulsion, Vol. 2, 2023, pp. 10.

[7] Désangles, V., Packan, D., Jarrige, J., Peterschmitt, S., Dietz, P., Scharmann, S., Holste, K., and Klar, P. J., "ECRA Thruster Advances: 30W and 200W Prototypes Latest Performances," Journal of Electric Propulsion, Vol. 2, No. 1, 2023, pp. 10.

[8] Ahedo, E. and Merino, M., "Two-Dimensional Supersonic Plasma Acceleration in a Magnetic Nozzle," Physics of Plasmas, Vol. 17, No. 7, 2010, pp. 073501.

[9] Horton, W., "Drift waves and transport," Reviews of Modern Physics, Vol. 71, No. 3, 1999, pp. 735.

[10] Garbet, X., "Turbulence in fusion plasmas: key issues and impact on transport modelling," Plasma physics and controlled fusion, Vol. 43, No. 12A, 2001, pp. A251.

[11] Koshkarov, O., Smolyakov, A., Raitses, Y., and Kaganovich, I., "Self-organization, structures, and anomalous transport in turbulent partially magnetized plasmas with crossed electric and magnetic fields," Physical review letters, Vol. 122, No. 18, 2019, pp. 185001.

[12] Moses, R., Gerwin, R., and Schoenberg, K., "Resistive plasma detachment in nozzle based coaxial thrusters," Proceedings Ninth Symposium on Space Nuclear Power Systems, Albuquerque, New Mexico, 1992, AIP Conference Proceedings No. 246, 1992, pp. 1293–1303.

[13] Olsen, C. S., Experimental characterization of plasma detachment from magnetic nozzles, Rice University, 2013.

[14] Little, J. and Choueiri, E., "Critical Condition for Plasma Confinement in the Source of a Magnetic Nozzle Flow," IEEE Transactions on Plasma Science, Vol. 43, No. 1, 2014, pp. 277–286.

[15] Tynan, G., Burin, M., Holland, C., Antar, G., and Diamond, P., "Radially sheared azimuthal flows and turbulent transport in a cylindrical helicon plasma device," Plasma physics and controlled fusion, Vol. 46, No. 5A, 2004, pp. A373.

[16] Yan, Z., Tynan, G., Holland, C., Xu, M., Müller, S., and Yu, J., "Shear flow and drift wave turbulence dynamics in a cylindrical plasma device," Physics of Plasmas, Vol. 17, No. 3, 2010.

[17] Xu, M., Tynan, G., Holland, C., Yan, Z., Muller, S., and Yu, J., "Fourier-domain study of drift turbulence driven sheared flow in a laboratory plasma," Physics of Plasmas, Vol. 17, No. 3, 2010.

[18] Burin, M., Tynan, G., Antar, G., Crocker, N., and Holland, C., "On the transition to drift turbulence in a magnetized plasma column," Physics of Plasmas, Vol. 12, No. 5, 2005.

[19] Thakur, S. C., Brandt, C., Cui, L., Gosselin, J., Light, A., and Tynan, G., "Multi-instability plasma dynamics during the route to fully developed turbulence in a helicon plasma," Plasma Sources Science and Technology, Vol. 23, No. 4, 2014, pp. 044006.

[20] Kamataki, K., Nagashima, Y., Shinohara, S., Kawai, Y., Yagi, M., Itoh, K., and Itoh, S.-I., "Coexistence of collisional drift and flute wave instabilities in bounded linear ECR plasma," journal of the physical society of japan, Vol. 76, No. 5, 2007, pp. 054501.

[21] Lee, P.-W., Lee, S.-W., and Chang, H.-Y., "Undriven periodic plasma oscillation in electron cyclotron resonance Ar plasma," Applied physics letters, Vol. 69, No. 14, 1996, pp. 2024–2026.

[22] Tsikata, S. and Minea, T., "Modulated electron cyclotron drift instability in a high-power pulsed magnetron discharge," Physical Review Letters, Vol. 114, 2015, pp. 185001.

[23] Ellison, C., Raitses, Y., and Fisch, N., "Cross-field electron transport induced by a rotating spoke in a cylindrical Hall thruster," Physics of Plasmas, Vol. 19, No. 1, 2012, pp. 013503.

[24] Smolyakov, A., Zintel, T., Couedel, L., Sydorenko, D., Umnov, A., Sorokina, E., and Marusov, N., "Anomalous electron transport in one-dimensional electron cyclotron drift turbulence," Plasma Physics Reports, Vol. 46, No. 5, 2020, pp. 496–505.

[25] Janhunen, S., Smolyakov, A., Chapurin, O., Sydorenko, D., Kaganovich, I., and Raitses, Y., "Nonlinear structures and anomalous transport in partially magnetized ExB plasmas," Physics of Plasmas, Vol. 25, 2018, pp. 11608.

[26] Anders, A., Ni, P., and Rauch, A., "Drifting localization of ionization runaway: Unraveling the nature of anomalous transport in high power impulse magnetron sputtering," Journal of Applied Physics, Vol. 111, No. 5, 2012.

[27] Carlsson, J., Kaganovich, I., Powis, A., Raitses, Y., Romadanov, I., and Smolyakov, A., "Particle-in-cell simulations of anomalous transport in a Penning discharge," Physics of Plasmas, Vol. 25, No. 6, 2018.

[28] Hepner, S., Wachs, B., and Jorns, B., "Wave-driven non-classical electron transport in a low temperature magnetically expanding plasma," Applied Physics Letters, Vol. 116, No. 26, 2020, pp. 263502.

[29] Takahashi, K., Charles, C., and Boswell, R. W., "Wave-driven electron inward transport in a magnetic nozzle," Scientific reports, Vol. 12, No. 1, 2022, pp. 20137.

[30] Maddaloni, D., Navarro-Cavallé, J., Merino, M., and Terragni, F., "Experimental investigation of oscillations in a magnetic nozzle," 35^{th} International Conference on Plasmas and Ionized Gases, Egmond aan Zee, The Netherlands, July 9–14, 2023.

[31] Takahashi, K., "Thirty Percent Conversion Efficiency from Radiofrequency Power to Thrust Energy in a Magnetic Nozzle Plasma Thruster," Scientific Reports, Vol. 12, 2022, pp. 18618.

[32] Olsen, C., Ballenger, M., Carter, M., Chang Diaz, F., Giambusso, M., Glover, T., Ilin, A., Squire, J., Longmier, B., Bering, E., and Cloutier, P., "Investigation of Plasma Detachment From a Magnetic Nozzle in the Plume of the VX-200 Magnetoplasma Thruster," Plasma Science, IEEE Transactions on, Vol. 43, No. 1, 2015, pp. 252–268.

[33] Gerwin, R. A., "Integrity of the plasma magnetic nozzle," Tech. rep., NASA/TP—2009-213439, 2009.

[34] Aanesland, A., Charles, C., Lieberman, M., and Boswell, R., "Upstream ionization instability associated with a current-free double layer," Physical review letters, Vol. 97, No. 7, 2006, pp. 075003.

[35] Hepner, S. T., The influence of instabilities on the electron dynamics of a Magnetic Nozzle, Ph.D. thesis, Department of Aerospace Engineering, The University of Michigan, Ann Arbor, MI, 2022.

[36] Doyle, S. J., Bennet, A., Tsifakis, D., Dedrick, J. P., Boswell, R. W., and Charles, C., "Characterization and control of an ion-acoustic plasma instability downstream of a diverging magnetic nozzle," Frontiers in Physics, Vol. 8, 2020, pp. 24.

[37] Singh, N., Rao, S., and Ranganath, P., "Waves generated in the plasma plume of helicon magnetic nozzle," Physics of Plasmas, Vol. 20, No. 3, 2013.

[38] Packan, D., Elias, P., Jarrige, J., Merino, M., Sánchez-Villar, A., Ahedo, E., Peyresoubes, G., Holste, K., Klar, P., Bekemans, M., Scalais, T., Bourguignon, E., Zurbach, S., Mares, M., Hooque, A., and Favier, P., "The MINOTOR H2020 project for ECR thruster development," 35^{th} International Electric Propulsion Conference, No. IEPC-2017-547, Electric Rocket Propulsion Society, 2017.

[39] Vialis, T., Jarrige, J., Aanesland, A., and Packan, D., "Direct thrust measurement of an electron cyclotron resonance plasma thruster," Journal of Propulsion and Power, Vol. 34, No. 5, 2018, pp. 1323–1333.

[40] Peterschmitt, S. and Packan, D., "Impact of the microwave coupling structure on an electron-cyclotron resonance thruster," Journal of Propulsion and Power, Vol. 37, No. 6, 2021, pp. 806–815.

[41] Kurzyna, J., Mazouffre, S., Lazurenko, A., Albarède, L., Bonhomme, G., Makowski, K., Dudeck, M., and Peradzyński, Z., "Spectral analysis of Hall-effect thruster plasma oscillations based on the empirical mode decomposition," Physics of Plasmas, Vol. 12, 2005, pp. 123506.

[42] Takahashi, K., Charles, C., and Boswell, R. W., "Wave-driven electron inward transport in a magnetic nozzle," Scientific Reports, Vol. 12, No. 1, 2022, pp. 12:20137.

[43] Light, M., Chen, F. F., and Colestock, P. L., "Low frequency electrostatic instability in a helicon plasma," Physics of Plasmas, Vol. 8, No. 10, 2001, pp. 4675–4689.

[44] Beall, J., Kim, Y., and Powers, E., "Estimation of wavenumber and frequency spectra using fixed probe pairs," Journal of Applied Physics, Vol. 53, No. 6, 1982, pp. 3933–3940.

[45] Petronio, F., Charoy, T., Alvarez Laguna, A., Bourdon, A., and Chabert, P., "Two-dimensional effects on electrostatic instabilities in Hall thrusters. II. Comparison of particle-in-cell simulation results with linear theory dispersion relations," Physics of Plasmas, Vol. 30, No. 1, 2023.

[46] Boni, F., Jarrige, J., Désangles, V., and Minea, T., "The curling probe: A numerical and experimental study. Application to the electron density measurements in an ECR plasma thruster," Review of Scientific Instruments, Vol. 92, 2021, pp. 033507.

[47] Boni, F., Désangles, V., and Jarrige, J., "A sheath correction method for electron density measurements with the microwave resonant curling probe," Plasma Sources Science and Technology, Vol. 32, No. 9, 2023, pp. 95018.

[48] Lumley, J. L., "The structure of inhomogeneous turbulent flows," Atmospheric turbulence and radio wave propagation, 1967, pp. 166–178.

[49] Sirovich, L., "Turbulence and the dynamics of coherent structures," Q. Appl. Math., Vol. XLV, 1987, pp. 561–590.

[50] Berkooz, G., Holmes, P., and Lumley, J. L., "The proper orthogonal decomposition in the analysis of turbulent flows," Ann. Rev. Fluid Mech., Vol. 25, 1993, pp. 539–575.

[51] Chatterjee, A., "An introduction to the proper orthogonal decomposition," Current Science, Vol. 78, 2000, pp. 808–817.

[52] Désangles, V., Shcherbanev, S., Charoy, T., Clément, N., Deltel, C., Richard, P., Vincent, S., Chabert, P., and Bourdon, A., "Fast camera analysis of plasma instabilities in hall effect thrusters using a POD method under different operating regimes," Atmosphere, Vol. 11, No. 5, 2020, pp. 1–18.

[53] Vincent, S., Dolique, V., and Plihon, N., "Nonlinear interactions of ion acoustic waves explored using fast imaging decompositions," Physics of Plasmas, Vol. 30, No. 1, 2023, pp. 1–13.

[54] Maddaloni, D., Domínguez-Vázquez, A., Terragni, F., and Merino, M., "Data-driven analysis of oscillations in Hall thruster simulations," Plasma Sources Science and Technology, Vol. 31, No. 4, 2022.

[55] Correyero, S., Jarrige, J., Packan, D., and Ahedo, E., "Plasma beam characterization along the magnetic nozzle of an ECR thruster," Plasma Sources Sci. Technol., Vol. 28, 2019, pp. 095004.

[56] Boni, F., Development of a microwave plasma diagnostic applied to electric propulsion systems, Ph.D. thesis, Université Paris-Saclay, 2022.

[57] Welch, P., "The use of fast Fourier transform for the estimation of power spectra: a method based on time averaging over short, modified periodograms," IEEE Transactions on audio and electroacoustics, Vol. 15, No. 2, 1967, pp. 70–73.

[58] Kim, Y. C. and Powers, E. J., "Digital bispectral analysis of self-excited fluctuation spectra," Physics of Fluids, Vol. 21, 1978, pp. 1452–1453.

[59] Hepner, S., Wachs, B., and Jorns, B. A., "Wave-driven non-classical electron transport in a low temperature magnetically expanding plasma," Applied Physics Letters, Vol. 116, No. 26, 2020, pp. 263502.

[60] Boeuf, J. and Garrigues, L., "Low frequency oscillations in a stationary plasma thruster," J. Applied Physics, Vol. 84, No. 7, 1998, pp. 3541–3554.

[61] Albarede, L., Mazouffre, S., Bouchoule, A., and Dudeck, M., "Low-frequency electron dynamics in the near field of a Hall effect thruster," Physics of Plasmas, Vol. 13, 2006, pp. 063505.

[62] Goebel, D. M., Jameson, K. K., Katz, I., and Mikellides, I. G., "Potential fluctuations and energetic ion production in hollow cathode discharges," Physics of Plasmas, Vol. 14, No. 10, 2007.

[63] Georgin, M. P., Jorns, B. A., and Gallimore, A. D., "Correlation of ion acoustic turbulence with self-organization in a low-temperature plasma," Physics of Plasmas, Vol. 26, No. 8, 2019.

[64] Dale, E. T. and Jorns, B. A., "Experimental characterization of Hall thruster breathing mode dynamics," Journal of Applied Physics, Vol. 130, No. 13, 2021, pp. 133302.

[65] Young, C., Fabris, A. L., MacDonald-Tenenbaum, N., Hargus, W., and Cappelli, M., "Time-resolved laser-induced fluorescence diagnostics for electric propulsion and their application to breathing mode dynamics," Plasma Sources Science and Technology, Vol. 27, No. 9, 2018, pp. 094004.

[66] Maddaloni, D., Domínguez-Vázquez, A., Terragni, F., and Merino, M., "Data-driven analysis of oscillations in Hall thruster simulations," Plasma Sources Science and Technology, Vol. 31, No. 4, apr 2022, pp. 045026.

[67] Fife, J., Martínez-Sánchez, M., and Szabo, J., "A Numerical Study of Low-Frequency Discharge Oscillations in Hall Thrusters," 33rd Joint Propulsion Conference, Seattle, WA, AIAA 97-3052, 1997.

[68] Giannetti, V., Saravia, M. M., Leporini, L., Camarri, S., and Andreussi, T., "Numerical and experimental investigation of longitudinal oscillations in Hall thrusters," Aerospace, Vol. 8, No. 6, 2021, pp. 148.

[69] Barral, S. and Ahedo, E., "Low-frequency model of breathing oscillations in Hall discharges," Physical Review E, Vol. 79, 2009, pp. 046401.

[70] Lafleur, T., Chabert, P., and Bourdon, A., "The origin of the breathing mode in Hall thrusters and its stabilisation," Journal of Applied Physics, Vol. 130, No. 5, 2021, pp. 053305.